Supplemental Materials for "Effective Hamiltonian for Photonic Topological Insulator with non-Hermitian Domain Walls"

Yandong Li,[1,*] Chongxiao Fan,[1,2,3,*] Xiaoyong Hu,[1,4,5,†] Yutian Ao,[1]
Cuicui Lu,[6,‡] C. T. Chan,[7,§] Dante M. Kennes,[2,3] and Qihuang Gong[1,4,5]

[1]*State Key Laboratory for Mesoscopic Physics & Department of Physics, Collaborative Innovation Center of Quantum Matter & Frontiers Science Center for Nano-optoelectronics, Beijing Academy of Quantum Information Sciences, Peking University, Beijing 100871, P. R. China*
[2]*Institute for Theory of Statistical Physics, RWTH Aachen University, and JARA Fundamentals of Future Information Technology, 52062 Aachen, Germany*
[3]*Max Planck Institute for the Structure and Dynamics of Matter, Center for Free Electron Laser Science, Hamburg, Germany*
[4]*Peking University Yangtze Delta Institute of Optoelectronics, Nantong, Jiangsu 226010, P. R. China*
[5]*Collaborative Innovation Center of Extreme Optics, Shanxi University, Taiyuan, Shanxi 030006, P. R. China*
[6]*Laboratory of Advanced Optoelectronic Quantum Architecture and Measurements of Ministry of Education, Beijing Key Laboratory of Nanophotonics and Ultrane Optoelectronic Systems, School of Physics, Beijing Institute of Technology, Beijing 100081, P. R. China*
[7]*Department of Physics, The Hong Kong University of Science and Technology, Clear Water Bay, Kowloon, Hong Kong, China*

CONTENTS

I. EFFECTIVE HAMILTONIANS FOR GAIN-LOSS DOMAIN WALLS IN OTHER SYSTEMS

We'll show that the phenomenon shown in the main text also appears in other systems. To be more specific, new states will emerge at gain-loss domain walls when we increase the difference of gain and loss between each region. We'll give effective Hamiltonians to describe the behaviors at gain-loss domain walls in other cases. Our main idea is, such phenomenon can be sufficiently described by considering the coupling of specific boundaries that make up the domain wall. The following examples are still based on topological models in order to make sure the stable existence of edge modes. However, this does not mean that our ideas only apply to the topological case and the edge modes in the one-dimensional(1D) case (or corner modes in the two-dimensional(2D) case). Related statements will be given in Sec. IV and V.

The Su-Schrieffer-Heeger model

The bulk Hamiltonian of the Su-Schrieffer-Heeger(SSH) model is given by

$$H_k = \begin{pmatrix} 0 & 1+ue^{ik} \\ 1+ue^{-ik} & 0 \end{pmatrix} \tag{S1}$$

Where u represents the intracell hopping coefficient, which is already normalized by the intercell coupling (see Fig. S1(a)). The model can be characterized by the bulk polarization p. When $u > 1$, $p = 1/2$, an open SSH chain will support topological protected edge modes. When $u < 1$, $p = 0$ and the model becomes trivial, no edge modes will appear at the end of an SSH chain.

When adding gains$(+i\gamma)$ and losses$(-i\gamma)$ to the left and the right parts of an open SSH chain (see Fig. S1(a)), we see no states in the gap in the trivial case ($u = 0.5$). For the topological case, there are four states in the bandgap (see Fig. S1(b)), while two of them are localized at the boundaries of the whole chain, just like the Hermitian case. The other two are domain-induced edge states that we care about, whose corresponding field distributions and eigen frequencies at different γs are given in Fig. S1(c) and (d).

The two domain-induced states can be described by an effective Hamiltonian with the form of Eq. (2) in the main text. Notice that edge states of an Hermitian SSH model should be zero-energy modes, the effective Hamiltonian can be written as

$$H_{\mathrm{SSH}}^{\mathrm{eff}} = \begin{pmatrix} 0+i\gamma & \kappa \\ \kappa^* & 0-i\gamma \end{pmatrix} \tag{S2}$$

Here κ is a fitting parameter. Fig. S1(d) shows the fitting results with $\kappa = \sqrt{3} = \sqrt{u^2-1}$. Eq. (S2) correctly describes the spectrum change of states we care about.

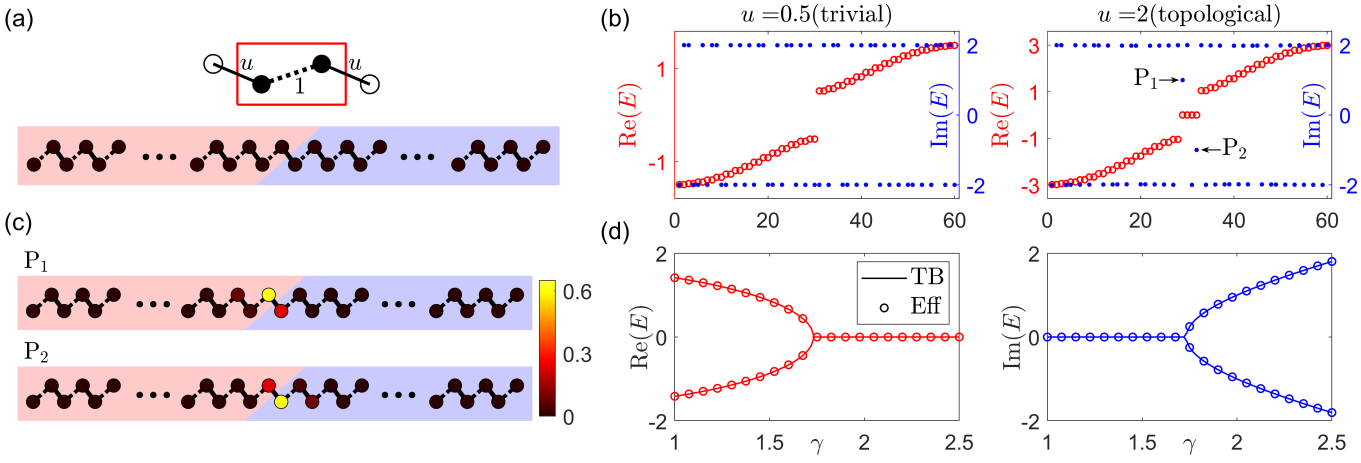

FIG. S1. (a) Unit cell of the SSH model and the configuration of SSH model with gain-loss domain walls: the left N_1 unit cells are experiencing gain $+\gamma$ while the other unit cells loss $-\gamma$. (b) Sorted spectra with $\gamma = 2$, $u = 0.5$, the trivial case and $u = 2$, the topological case. (c) Field distributions of domain-induced edge states $P_{1,2}$. (d) Eigenenergies of $P_{1,2}$ under different γs. Solid lines represent results given by the tight-binding model, circles represent the fitting results.

The valley-typed photonic topological insulator

The bulk Hamiltonian of the valley-typed PTI [1] is given by

$$H(\boldsymbol{k}) = \begin{pmatrix} m & t(1+e^{i\boldsymbol{k}\cdot\boldsymbol{a}_1}+e^{i\boldsymbol{k}\cdot\boldsymbol{a}_2}) \\ t(1+e^{-i\boldsymbol{k}\cdot\boldsymbol{a}_1}+e^{-i\boldsymbol{k}\cdot\boldsymbol{a}_2}) & -m \end{pmatrix} \tag{S3}$$

Here $\boldsymbol{k}=(k_x,k_y)$ is the Bloch wave vector, $\boldsymbol{a}_1=(1,0),\boldsymbol{a}_2=(1/2,\sqrt{3}/2)$ are two lattice translation vectors (see the upper plots of Fig. S2(a)). For $m\neq 0$, the Hamiltonian always has a component $m\hat{\sigma}_z$ ($\hat{\sigma}_z$ denotes the Pauli matrix), which breaks the sublattice symmetry, leading to the nontrivial topology of the system. This kind of photonic crystal corresponds to the valley Hall effect in the electronic system and can be characterized by the valley Chern number.

To study the domain-induced edge states, we consider a valley photonic crystal with a periodic boundary condition along $\boldsymbol{a}_2$, while the crystal translation symmetry is broken along the direction perpendicular to $\boldsymbol{a}_2$. The bottom plot of Fig. S2(a) shows the supercell of such a crystal. A gain-loss domain wall is setted by adding gaines$(+i\gamma)$ to the left part of the chain while adding losses$(-i\gamma)$ to the remaining part. The projection band structure is shown in Fig. S2(b) and the domain-induced edge bands are colored in red. Their corresponding field distributions of two chosen states $\mathrm{P}_{1,2}$ are exhibited in Fig. S2(c), which have similar properties with the results of the SSH model mentioned above and the AAH model mentioned in the main text.

The effective Hamiltonian in this case also has the form of Eq. (2) in the main text.

$$H^{\mathrm{eff}}_{\mathrm{valley}} = \begin{pmatrix} \omega_1+i\gamma & \kappa \\ \kappa^* & \omega_2-i\gamma \end{pmatrix} \approx \begin{pmatrix} m+i\gamma & \kappa \\ \kappa & -m-i\gamma \end{pmatrix} \tag{S4}$$

Fig. S2(d) shows the edge spectrum given by the tight-binding model and the above effective Hamiltonian. Here the coupling coefficient κs at different ks are determined following the same scheme in the main text (see Eq. (3) and (4)).

The C_{6v}-typed photonic topological insulator

The bulk Hamiltonian of the C_{6v}-typed (or pseudo-spin-typed) PTI [2] is given by

$$H(\boldsymbol{k}) = \begin{pmatrix} 0 & 1 & 0 & te^{i\boldsymbol{k}\cdot\boldsymbol{a}_1} & 0 & 1 \\ 1 & 0 & 1 & 0 & te^{i\boldsymbol{k}\cdot\boldsymbol{a}_2} & 0 \\ 0 & 1 & 0 & 1 & 0 & te^{i\boldsymbol{k}\cdot\boldsymbol{a}_3} \\ te^{-i\boldsymbol{k}\cdot\boldsymbol{a}_1} & 0 & 1 & 0 & 1 & 0 \\ 0 & te^{-i\boldsymbol{k}\cdot\boldsymbol{a}_2} & 0 & 1 & 0 & 1 \\ 1 & 0 & te^{-i\boldsymbol{k}\cdot\boldsymbol{a}_3} & 0 & 1 & 0 \end{pmatrix} \tag{S5}$$

Here $\boldsymbol{k}=(k_x,k_y)$ is the Bloch wave vector, $\boldsymbol{a}_1=(0,1),\boldsymbol{a}_2=(\sqrt{3}/2,1/2)$ are two lattice translation vectors, $\boldsymbol{a}_3=\boldsymbol{a}_2-\boldsymbol{a}_1$ is an auxiliary vector (see upper plots of Fig. S3(a)). t represents the intracell hopping coefficient (which has been normalized by the

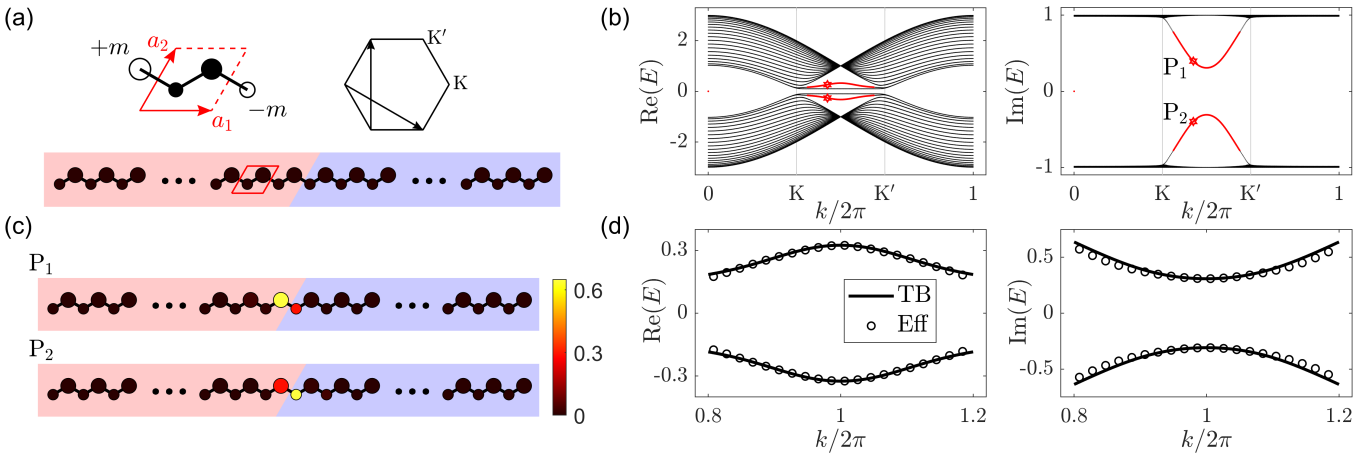

FIG. S2. (a) Unit cell, the first Brillouin zone of the valley-typed PTI and the supercell of such PTI with a gain-loss domain wall (b) Projection band structure along $\boldsymbol{a}_2$ with $m=0.1,t=1,\gamma=1$. (c) The corresponding field distributions of 2 representative states $\mathrm{P}_{1,2}$. (d) Dispersion relations of two domain-induced edge states. Solid lines represent results given by the tight-binding model, circles represent the fitting results.

intercell hopping coefficient). When changing the hopping strength from $t < 1$ to $t > 1$, a band reverse will occur at Γ point, leading to a phase translation from trivial to topological. This kind of photonic crystal corresponds to the spin Hall effect in electronic systems and can be characterized by the spin Chern number.

To study the domain-induced edge states, we consider a C_{6v}-typed photonic crystal with a periodic boundary condition along $\boldsymbol{a}_1$, while the crystal translation symmetry is broken along the direction perpendicular to $\boldsymbol{a}_1$. This kind of boundary is named as 'zigzag' boundary (for the periodic boundary condition along the direction perpendicular to $\boldsymbol{a}_1$, it is named as 'armchair' boundary). The bottom plot of Fig. S3(a) shows the supercell of such a crystal with zigzag boundary. The gain-loss domain wall is constructed by using the same method as above. Fig. S3(b) shows projection band structures with $\gamma = 3$, and $t = 1/2$ (trivial), $t = 3$ (topological), respectively. The domain-induced bands are colored in red. In the trivial case, the domain wall cannot result in any new states, while in the topological case, four bands appear in the bandgap. These bands correspond to domain-induced edge states and the field distributions of four representative states P_{1-4} are shown in Fig. S3(c). They have similar properties to models mentioned before.

To write the effective Hamiltonian, notice that the edge states of a C_{6v}-typed PTI can also be understood by considering the dimer limit, that is, $t \to \infty$. In such limit, the behaviors at the domain wall are only determined by the four sites that make up it. With this in mind, we write the effective Hamiltonian

$$H^{\mathrm{eff}}_{C_{6v}} = \begin{pmatrix} i\delta & u & 0 & we^{ik} \\ u & -i\delta & w & 0 \\ 0 & w & -i\delta & u \\ we^{-ik} & 0 & u & i\delta \end{pmatrix} \tag{S6}$$

Here δ, u, w are all fitting parameters. Fig. S3(d) compares the fitting results and the dispertion relations given by the tight-binding model, which implies the right form of Eq. (S6).

We have shown the domain-induced states and given corresponding effective Hamiltonians in 3 other systems. In the topological cases, gain-loss domain walls in these models can support localized modes, while in the trivial cases they cannot. This is because in the trivial cases, no modes will appear at the boundaries of a subsystem. Again, we emphasize that, we use topological models only because they can provide stable boundary states without tedious parameter adjustment. The evolution process of domain-induced states is only a PT-phase transition and has nothing to do with topological phase transition. However, if the related Hermitian system is topological, we can say that the existence of such domain-induced states are protected by the topology of the corresponding Hermitian topology, since disorders do not affect the existence of boundary modes in each subsystem.

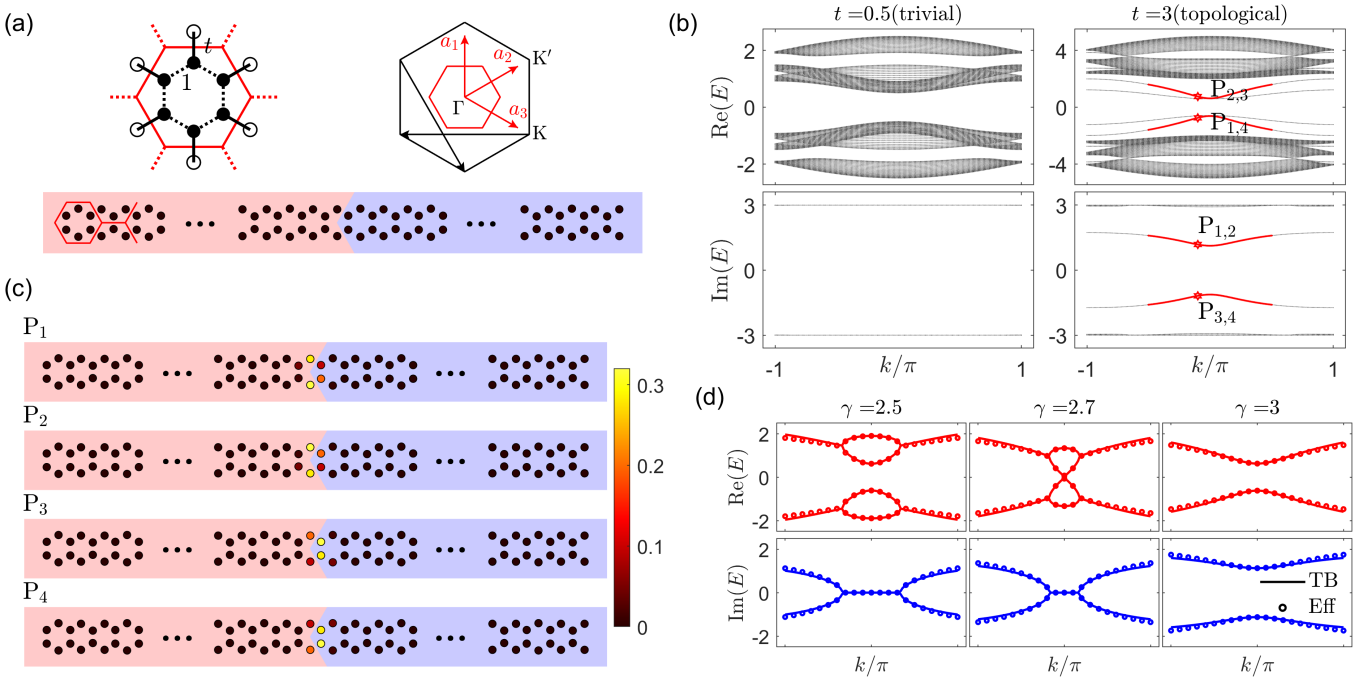

FIG. S3. (a) Unit cell, the first Brillouin zone of the C_{6v}-typed PTI and the supercell of such PTI with a gain-loss domain wall (b) Projection band structure along $\boldsymbol{a}_1$ with $\gamma = 3$, $t = 0.5$ (trivial) and $t = 3$ (topological). In the trivial, the gain-loss domain wall does not support any localized states. (c) The corresponding field distributions of s representative states P_{1-4}. (d) Dispersion relations of four domain-induced edge states. Solid lines represent results given by the tight-binding model, circles represent the fitting results.

II. FITTING PROCESSES OF THE AAH MODEL

The effective Hamiltonians of 1D AAH chain and 2D AAH model with cross-shaped domain walls are given by

$$H_{1D}^{\text{eff}} = \begin{pmatrix} \omega_1 + i\gamma & \kappa \\ \kappa^* & \omega_2 - i\gamma \end{pmatrix}, \qquad H_{2D}^{\text{eff}} = \begin{pmatrix} \omega_1 - i\gamma & \kappa_{12} & \kappa_{13} & \kappa_{14} \\ \kappa_{21} & \omega_2 + i\gamma & \kappa_{23} & \kappa_{24} \\ \kappa_{31} & \kappa_{32} & \omega_3 - i\gamma & \kappa_{34} \\ \kappa_{41} & \kappa_{42} & \kappa_{43} & \omega_4 + i\gamma \end{pmatrix} \tag{S7}$$

As the dimension of the effective Hamiltonian increases, the parameters to be determined increase with the speed of $O(n^2)$. For example, for 1D case we only have to fit one parameter, while in 2D case we actually need to do a six-dimensional fitting (except the diagonal terms). To avoid this, we introduce a new parameter λ, and the relation between κs and λ is given by $\kappa_{ij} = \langle \varphi_i | H|_{\gamma=0} | \varphi_j \rangle$ (see Eq. (3) and (4) in the main text). Here, κs are independent of γ, which is based on the following considerations. Take the 1D case as an example. Even if we calculate $\kappa(\lambda) = \langle \varphi_G | H_{1D} | \varphi_L \rangle = \sum_{n,m} \varphi_G^*(n) \varphi_L(m) H_{1D}^{nm}$, we find that the non-Hermitian modification is at least two orders lower than the Hermitian contributions. So it is reasonable to use the Hermitian Hamiltonian to calculate κs.

Fig. S4(a) shows the relationship between the eigenenergy of the domain-induced edge states and γ at different ϕ. The results given by the tight-binding model are shown with the red solid line. We test different λs and the results (which are shown with colorful dashed line) show that $\lambda = 9$ is a good choice for $\phi/\pi = 5/3$ and $5.15/3$. As a further approximation, we could set $\lambda = 9$ for all ϕs. Fig. S4(b) shows the dispersion relation in ϕ dimension at $\gamma/t = 0.8,\ 1.2$. The results given by the tight-binding calculation are shown in red solid lines, while the results given by the two-level effective Hamiltonian (Eq. (2) in the main text) are shown in the green solid line. The effective Hamiltonian reflects the behavior at the domain wall exactly.

For the 2D AAH lattice with cross-shaped domain walls, we use the $E - \gamma$ relation at $\phi_x/\pi = \phi_y/\pi = 1/3$ and $1/3 + 0.05$ to test the effect of different λ and the results are exhibited in Fig. S5(a). We can see that $\lambda = 9.5$ shows a good performance. In Fig. S5(b), we show the dispersion relation given by the tight-binding Hamiltonian H_{2D} (colored in red) and the effective Hamiltonian H_{2D}^{eff}. The results of these two methods agree quite well.

We point out that some small errors in the fitting results may be generated from:

i. Actually we should use different λs for different ϕs.

ii. When we construct exponentially localized corner states, we introduce an exceptional decay with form of $e^{-\lambda \bar{\alpha} r}$ for each ψ, that is, we include all the bulk properties in $\bar{\alpha}$ and λ is only a fitting parameter, which may lead to some errors.

iii. The cross-shaped domain walls also lead to other domain-induced states besides the 4 corner states we focused on (see Sec. IV). These 4 domain-induced corner states are also coupled with other types of domain-induced states, which means the complete effective Hamiltonian should contain all of such states.

Although the fitting method will lead to some errors, it is undeniabe that the introduction of λ greatly reduces the workload of fitting in high dimensional cases. At the same time, it also achieves good fitting.

In conclusion, by introduing λ, we successfully turned a six dimensional fitting into a one dimensional fitting. The fitting results do have some errors (the relative error is on the order of $10^{-2} \sim 10^{-1}$) and some possible reasons are listed above.

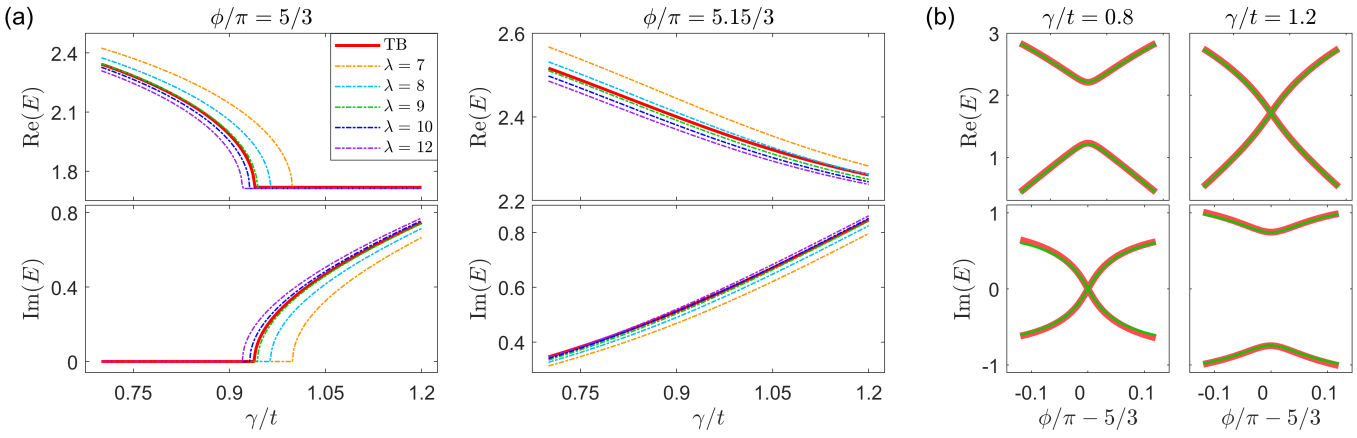

FIG. S4. (a) Comparison of the $E - \gamma$ relation between the one given by the full tight-binding model and those given by our effective Hamiltonian with different λs, at $\phi/\pi = 5/3$ and $5.15/3$. (b) Comparison of the dispersion relation between the one given by the full tight-binding model (red) and the one given by our effective Hamiltonian with $\lambda = 9$ (green).

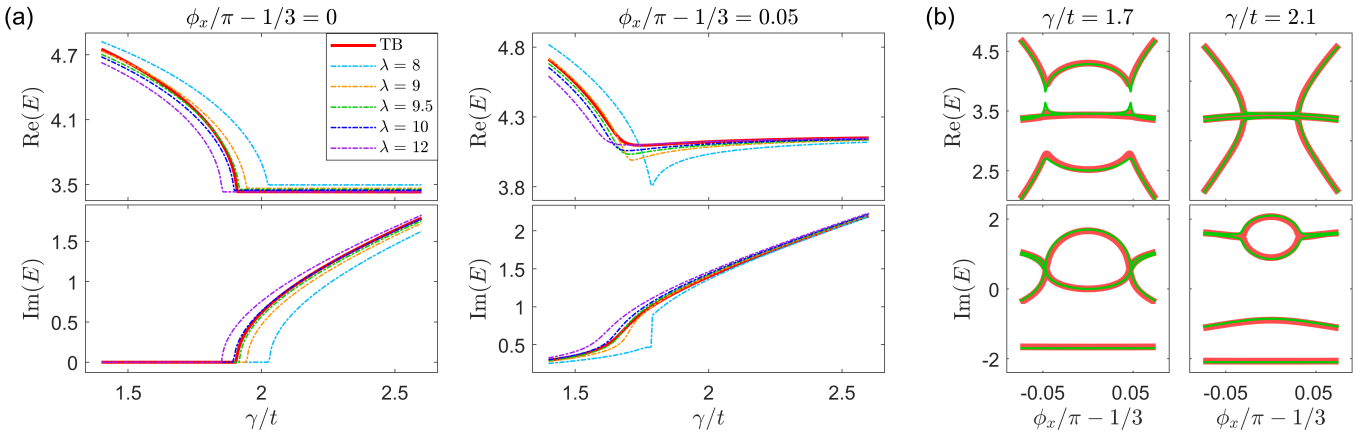

FIG. S5. ((a) Comparison of the $E-\gamma$ relation between the one given by the full tight-binding model and those given by our effective Hamiltonian with different λs, at $\phi_x/\pi = \phi_y/\pi = 1/3$ and $1/3+0.05$. (b) Comparison of the dispersion relation between the one given by the full tight-binding model (red) and the one given by our effective Hamiltonian with $\lambda = 9.5$ (green) at $\gamma/t = 1.7, 2.1$.

However, it is no doubt that these effective Hamiltonians give the correct physics. At the very least, we provide a basic form approximate values of the parameters, which provides a good basis for more accurate fitting, if necessary.

III. BAND TOPOLOGY OF THE AAH MODEL

In this section, we'll briefly introduce the band topology of the 1D and 2D Hermitian AAH model.

A Hermitian 1D AAH model (the Hamiltonian is given by Eq. (1) in the main text, with $\gamma_n = 0$) can be treated as a 2D lattice with a synthetic ϕ dimension with $\phi \in [0, 2\pi)$. Using the Fourier transformation $c_n^\dagger = \sum_m e^{im\phi} c_{n,m}^\dagger$, we can write the Hamiltonian as [3]

$$h_{\mathrm{1D,syn}} = \sum_m \left[\sum_{n=1}^{N} \frac{V}{2} e^{i2\pi\beta(n-q)} c_{n,m}^\dagger c_{n,m+1} + \sum_{n=1}^{N-1} t c_{n,m}^\dagger c_{n+1,m} + h.c. \right] \tag{S8}$$

It can be seen that there is an equivalent perpendicular magnetic field with β quantum flux per unit cell, which means the corresponding topology can be described by the Chern number. In the case $\beta = 1/3$, the model has translation symmetries in both real-space and ϕ-space, one can give the bulk Hamiltonian

$$h(k,\phi) = \begin{pmatrix} V\cos(-2\pi/3+\phi) & t & te^{ika} \\ t & V\cos\phi & t \\ te^{-ika} & t & V\cos(2\pi/3+\phi) \end{pmatrix} \tag{S9}$$

Here k is the Bloch wave vector in the real-space and a is the length of the real-space unit cell. By calculating the Chern number as

$$C^n = \frac{1}{2\pi i} \int_{-\pi/a}^{\pi/a} dk \int_0^{2\pi} d\phi \;\; \nabla \times \langle u_{k,\phi}^n | \nabla | u_{k,\phi}^n \rangle \tag{S10}$$

where $|u_{k,\phi}^n\rangle$ satisfies $h(k,\phi)|u_{k,\phi}^n\rangle = \varepsilon_n |u_{k,\phi}^n\rangle$, we get $C^1 = 1, C^2 = -2, C^3 = 1$. The gap Chern number is given by $C_{\mathrm{gap}}^1 = C^1 = 1, C_{\mathrm{gap}}^2 = C^1 + C^2 = -1$, which implies the nontrivial band topology.

For the 2D Hermitian case, the system can be treated as the direct product of two 1D AAH chains, namely, $H_{\mathrm{2D}} = I_y \otimes h_{\mathrm{1D},x} + h_{\mathrm{1D},y} \otimes I_x$. Here $I_{x,y}$ are indentity matrixs with suitable sizes and $h_{\mathrm{1D},x(y)}$ is the 1D AAH Hamiltonian with parameters $N_{x(y)}, V_{x(y)}, \beta_{x(y)}$ and $\phi_{x(y)}$. This implies the eigenstate and the corresponding eigenenergy satisfy $|\psi_{\mathrm{2D}}\rangle = |\chi_{\mathrm{1D},x}\rangle \otimes |\chi_{\mathrm{1D},y}\rangle$ and $E_{\mathrm{2D}} = \varepsilon_{\mathrm{1D},x} + \varepsilon_{\mathrm{1D},y}$, where $H|\psi\rangle = E|\psi\rangle$, $h_{x(y)}|\chi_{x(y)}\rangle = \varepsilon_{x(y)}|\chi_{x(y)}\rangle$ (for simplification, we'll use H, $|\psi\rangle$ and E to represent the Hamiltonian, eigenstates and eigenenergies of the 2D model while h, $|\chi\rangle$ and ε for the 1D case in this section). The above mathematics gives us a simple principle to determine an eigenstate of the 2D AAH model. It shows that a 2D edge state is always the direct product of $|\chi^{\mathrm{edge}}\rangle$ and $|\chi^{\mathrm{bulk}}\rangle$. Besides, a 2D corner state always has the form of $|\chi^{\mathrm{edge}}\rangle \otimes |\chi^{\mathrm{edge}}\rangle$. The other combinations will result in the 2D bulk states.

Fig. S6(c) shows the spectrum confined on plane $\phi_x = \phi_y$ of a 2D AAH model with parameters $N_x = N_y = 30, V_x = V_y = 3$ and $\beta_x = \beta_y = 1/3$ (the same with the main text). The corresponding $h_{x,y}$ are the same with each other, and its spectrum

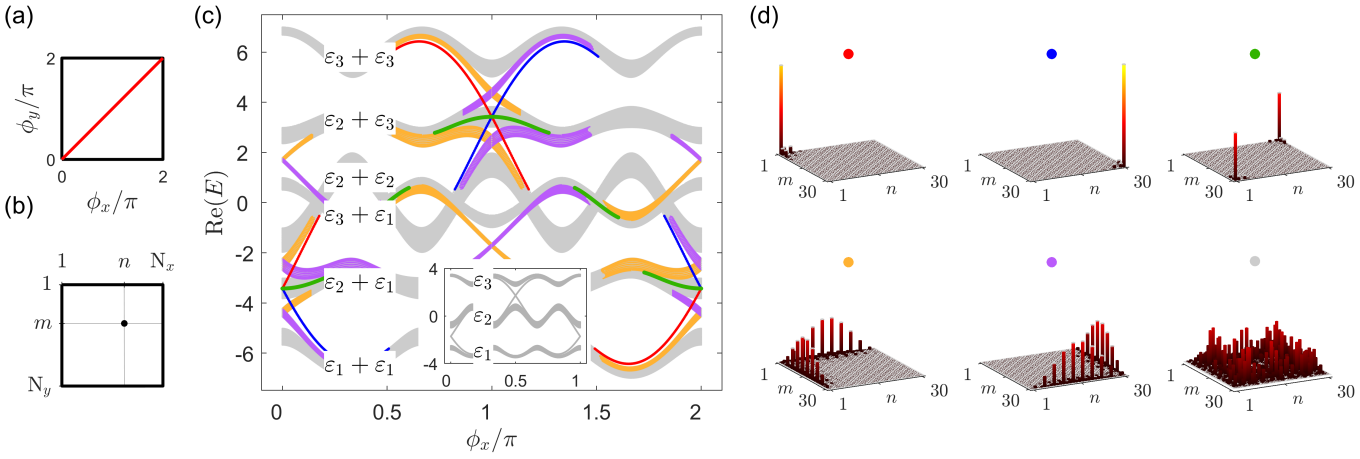

FIG. S6. The whole spectrum of a Hermitian 2D AAH lattice with $N_x = N_y = 30, V_x = V_y = 3, \beta_x = \beta_y = 1/3$ on the plane $\phi_x = \phi_y$. (a) Schematic diagram of the cross section in the ϕ space. (b) Schematic diagram of the 2D AAH model, we use (n,m) to mark a certain site, where $n = 1,2,3,\cdots,N_x$, $m = 1,2,3,\cdots,N_y$. (c) The spectrum on the cross section shown in (a). Different kind of states are colored in different colors: corner states (red, blue and green), edge states (orange and purple), bulk states (gray). Inner plot: the spectrum of the corresponding 1D AAH model $H_{\mathrm{1D},x}$. It has 3 bulk bands and we label them $\varepsilon_{1,2,3}$. (d) Corresponding representative field distributions of different kinds of states, the six subfigures do not share the same colorbar.

is shown in the inner plot of Fig. S6(c). We label the bulk bands $\varepsilon_{1,2,3}$ with $\varepsilon_1 < \varepsilon_2 < \varepsilon_3$. According to the adding rule of eigenenergies, the 5 bulk bands of the 2D spectrum are composed of $\varepsilon_{1,x}+\varepsilon_{1,y}$, $\varepsilon_{1,x(y)}+\varepsilon_{2,y(x)}$, $\varepsilon_{2,x}+\varepsilon_{2,y}$ and $\varepsilon_{1,x(y)}+\varepsilon_{3,y(x)}$, $\varepsilon_{2,x(y)}+\varepsilon_{2,y(x)}$, $\varepsilon_{3,x}+\varepsilon_{3,y}$, respectively, in the ascending order of energies. Different kinds of states are colored in different colors and the corresponding field distributions are exhibited in Fig. S6(d). One may ask why there are only two types of edge states, the one colored in orange localize at edges $n=1$ and $m=1$ at the same time, while the other one colored in purple localize at edges $n=30$ and $m=30$. Well, there were actually four kinds of edge states, $|\chi^{\text{edge}}_{x,n=1}\rangle\otimes|\chi^{\text{bulk}}_{y}\rangle$, $|\chi^{\text{bulk}}_{x}\rangle\otimes|\chi^{\text{edge}}_{y,m=1}\rangle$, $|\chi^{\text{edge}}_{x,n=30}\rangle\otimes|\chi^{\text{bulk}}_{y}\rangle$, $|\chi^{\text{bulk}}_{x}\rangle\otimes|\chi^{\text{edge}}_{y,m=30}\rangle$. However, $h_{x,y}$ have the same spectrum, which implies that the first two states and the last two states are both double degenerate. Also, there are only three types of corner states, which is casued by the degenerate of $|\chi^{\text{edge}}_{x,n=1}\rangle\otimes|\chi^{\text{edge}}_{y,m=30}\rangle$ and $|\chi^{\text{edge}}_{x,n=30}\rangle\otimes|\chi^{\text{edge}}_{y,m=1}\rangle$.

Just as the 1D AAH chain reflects the properties of a 2D Chern insulator, the 2D AAH lattice also reflects the properties of a four-dimensional (4D) Chern insulator with two synthetic dimensions (ϕ_x,ϕ_y). The 4D Chern number can be written as the product of two 2D Chern numbers, namely, $C^{\varepsilon_m+\varepsilon_n}_{\text{4D}} = C^{\varepsilon_m}_{\text{2D},x}\times C^{\varepsilon_n}_{\text{2D},y}$. It's easy to calculate the band Chern number as $C_{\text{4D}}=\{1,-4,6,-4,1\}$ and the gap Chern number as $\{1,-3,3,-1\}$ in the ascending order of energies. The non-zero gap Chern number implies the nontrivial band topology of the 2D AAH lattice [4].

IV. WHOLE SPECTRUMS OF THE 2D NON-HERMITIAN AAH LATTICE IN THE MAIN TEXT

In the main text, we focused on corner states induced by gain-loss domains, so we just showed a small region of the spectrum. In this section, we'll give the whole spectrum on the $\phi_x=\phi_y$ plane. Besides, we'll show that the cross-shaped domain wall in the main text also supports other localized staes.

In Fig. S7, we show the whole spectrum of the non-Hermitian 2D AAH lattice with the same parameters as Fig. 3 in the main text ($\gamma/t=1.7$) on the plane $\phi_x=\phi_y$. The spectrum and four colored bands in the red box are just what we have exhibited in Fig. 3(b) in the main text. We also find a similar structure at the neighborhood of $\phi_x=\phi_y=4\pi/3$, which is highlighted by a light-blue box. These domain-induced corner states at $\phi_x=\phi_y=4\pi/3$ originate from the combination of 1D domain-induced edge modes with energies $\varepsilon<0$. To further illustrate our classification rules of the domain-induced corner modes, Fig. S8 gives field distributions of more representative states. In the neighboring of $\phi_x=\phi_y=\pi/3$, the PT-broken or unbroken phase is the main principle of classification (see Q_{a1}, Q_{b1} and Q_{b2}). While away from the center, we focuse on the asymmetric between Domain II and IV (see Q_{b3}, Q_{b4}). In other words, we actually use two principles to classify the bands in different regions, although the influence of these two principles may exist at the same time (see Q_{a2}, Q_{a3}). This is why the imaginary part of the green band in Fig. S8(b) is discontinuous. However, one can see from the exhibited field distributions that, our classification does reflect the main characteristics of different regions.

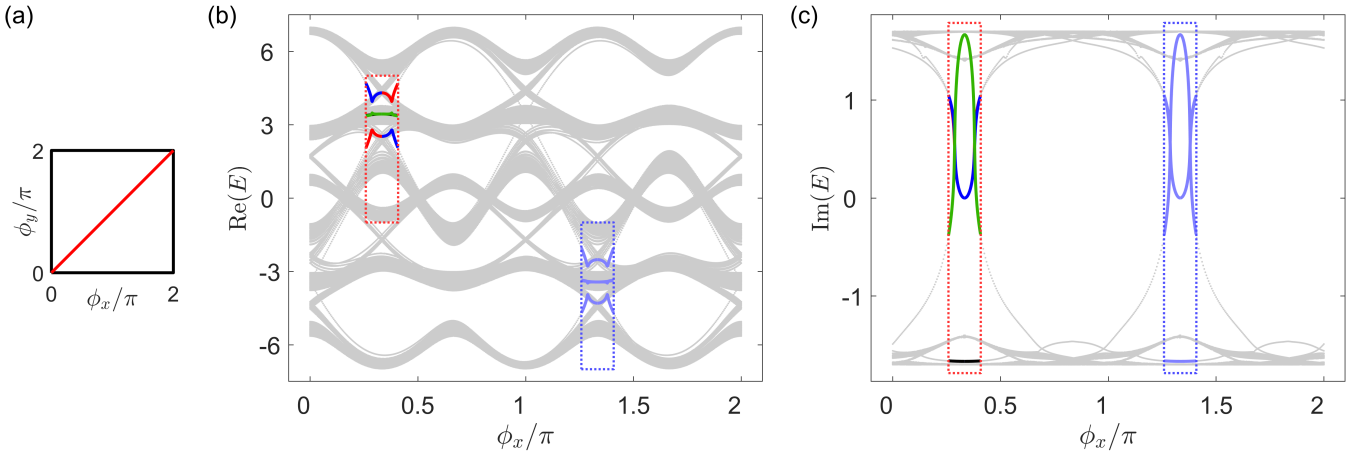

FIG. S7. The whole spectrum of a non-Hermitian 2D AAH lattice with $N_x=N_y=30, N_1=N_2=16, V_x=V_y=3, \beta_x=\beta_y=1/3$ and $\gamma/t=1.7$ on the plane $\phi_x=\phi_y$. (a) Schematic diagram of the cross section in the ϕ space. (b), (c) The real and imaginary spectrums on the cross section shown in (a). The red box shows the region exhibited in Fig. 3(a) in the main text. The blue box gives a region where there's a similar structure as in the red box.

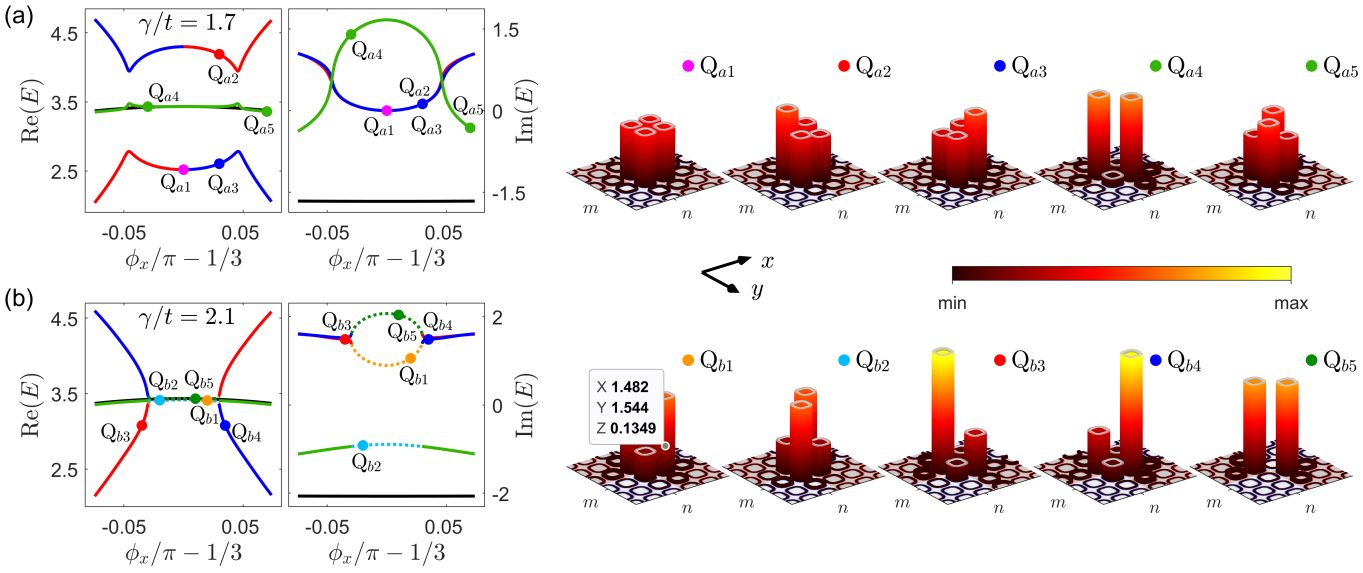

FIG. S8. Corner bands shown in Fig. 3(b) in the main text and field distributions of more representative states. Four bands are classified based on the PT phase in the middle region. Away from the middle, the four bands are classified based on the asymmetric between Domain II and IV.

By comparing the spectrum of 2D AAH lattice with cross-shaped non-Hermitian domain walls (Fig. S7(b)) with the Hermitian case (Fig. S6(c)), we find that certain bands appear in bandgaps at the neighborhood of $\phi_x = \phi_y = \pi/3$ and $4\pi/3$. In addition to domain-induced corner states, these certain bands also represent domain-induced edge states. Fig. S9(a) shows the configuration of our 2D AAH lattice, four domain walls are labeled as ①–④ for convenient description. There are two kinds of domain-induced edge states. The corresponding fields localize at either domain walls ①, ② at the same time (colored in red) or ③, ④ at the same time (colored in blue). These states are generated from the coupling of edges channels of the four individual subsystems I–IV. To verify this, we count the number of domain-induced edge states, the results show that there are 56 red states and 48 blue states for each proper ϕ_x. These numbers can be explained through counting the number of edge channels belonging to related subsystems. Take states colored in red as an example, which can be understood by the coupling of edge channels belonging to subsystem II and subsystems I, III (see Fig. S9(b)). Subsystem II (with size $N_1 \times N_2$) has $(N_1 - 2) + (N_2 - 2) = 28$ edge channels, which locate at edges $m = N_1$ and $n = N_2$. Meanwhile, subsystem I has $N_1 - 2 = 14$ edges channels localize at edge

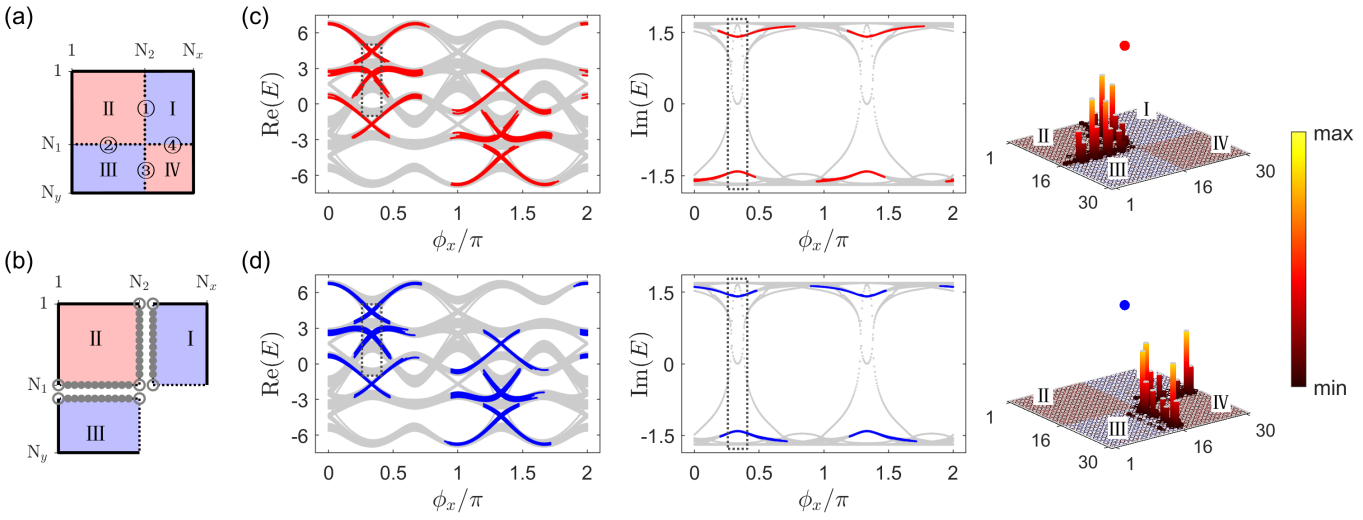

FIG. S9. Domain-induced edge states in a non-Hermitian 2D AAH lattice with $N_x = N_y = 30, N_1 = N_2 = 16, V_x = V_y = 3, \beta_x = \beta_y = 1/3$ and $\gamma/t = 1.7$. (a) The configuration of our 2D AAH lattice with cross-shaped domain walls. (b) Schematic diagram for how to count the number of domain-induced edge states colored in red. the number of edge states of a separated subsystem is determined by the number of gray solid dots. (c) The real and imaginary spectrums for two types of domain-induced edge states on plane $\phi_x = \phi_y$. The black box shows the region exhibited in Fig. 3(a) in the main text. (d) Corresponding representative field distributions of different kinds of states.

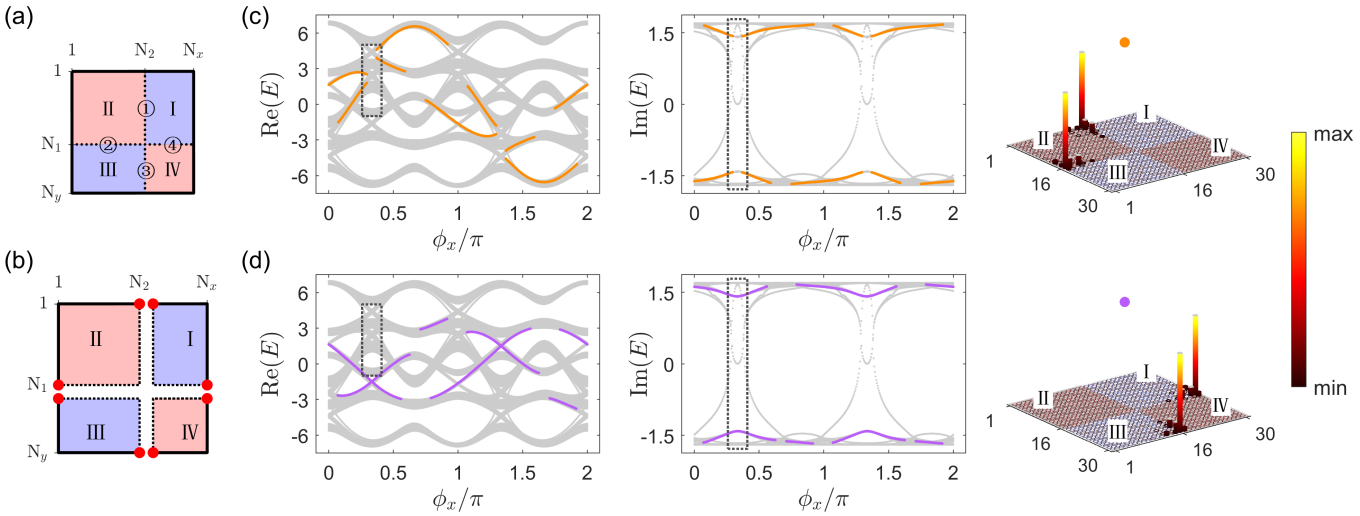

FIG. S10. 'Corner' states in a non-Hermitian 2D AAH lattice with $N_x = N_y = 30, N_1 = N_2 = 16, V_x = V_y = 3, \beta_x = \beta_y = 1/3$ and $\gamma/t = 1.7$ induced by non-Hermitian domains and the boundary of the whole system. (a) The configuration of our 2D AAH lattice with cross-shaped domain walls. (b) 8 original corner states which take part in the process of generating such domain-induced 'corner' states. (c) The real and imaginary spectrums for two types of domain-induced 'corner' states on plane $\phi_x = \phi_y$. The black box shows the region exhibited in Fig. 3(a) in the main text. (d) Corresponding representative field distributions of different kinds of states.

$n = N_2 + 1$, subsystem III has $N_2 - 2 = 14$ edges channels localize at edge $m = N_1 + 1$. These channels take part in the process of generating the domain-induced edge states colored in red, so we get 56 such states in total.

There are also 8 states localize around the intersection points of domain walls ①–④ and the boundary of the whole system, just as we exhibit in Fig. S10. These states are also domain-induced 'corner' states since they are generated from the coupling of corner state belonging to four subsystems (and the vacuum). Fig. S10(b) shows 8 corner states belonging to 4 individual subsystems, which take part in the process of generating such domain-induced 'corner' states.

One last thing to add, notice there are only two types of domain-induced edge states and 'corner' states. This is due to the 2-fold degeneration we explained in the previous subsection. In more general cases, there will be four types of domain-induced edge states (or 'corner' states) which locate at domain wall ①, ②, ③ or ④ (or its intersection point with the boundary of the whole system), respectively.

V. GAIN-LOSS DOMAIN WALLS WITH DIFFERENT POSITIONS AND SHAPES

We have constructed complex domain walls in Fig. 5 in the main text. Also, we have shown that this configuration support domain-induced corner states in different subspace of the whole phasespace. In this section, we'll show how to determine the subspace that supports domain-induced corner states and give the corresponding spectrums. Also, we'll show some examples, in which case the gain-loss domain walls are no longer cross-shaped, to verify the validity of our method to construct effective Hamiltonians in broader cases. Finally, we'll show that the effective Hamiltonian may provide guidance for us to study certain physics in domain-wall-configurations. For example, a third-order exceptional point(EP3) composed of domain-induced corner states can be designed based on the effective Hamiltonian.

Determine the subspace that supports domain-induced corner states

In the non-Hermitian AAH model, the direct product form of the 2D Hamiltonian no longer applies, and we cannot write $|\psi\rangle = |\chi_x\rangle \otimes |\chi_y\rangle$. However, the differences $(H^{\mathrm{NH}} - I_y \otimes h_x^{\mathrm{NH}} - h_y^{\mathrm{NH}} \otimes I_x)$ are just caused by the on-site imaginary potential with the form of $\mathrm{diag}\{i\gamma_1, i\gamma_2, i\gamma_3, \cdots, i\gamma_{N_y \times N_x}\}$, which can be treated as a pertubation. So, we have every reason to believe that if there's a 1D domain-induced edge state at ϕ_{x_0} with energy E_1 and another 1D domain-induced edge state at ϕ_{y_0} with energy E_2, there must be a 2D domain-induced corner state appears at the neighborhood of (ϕ_{x_0}, ϕ_{y_0}), and with energy around $E_1 + E_2$.

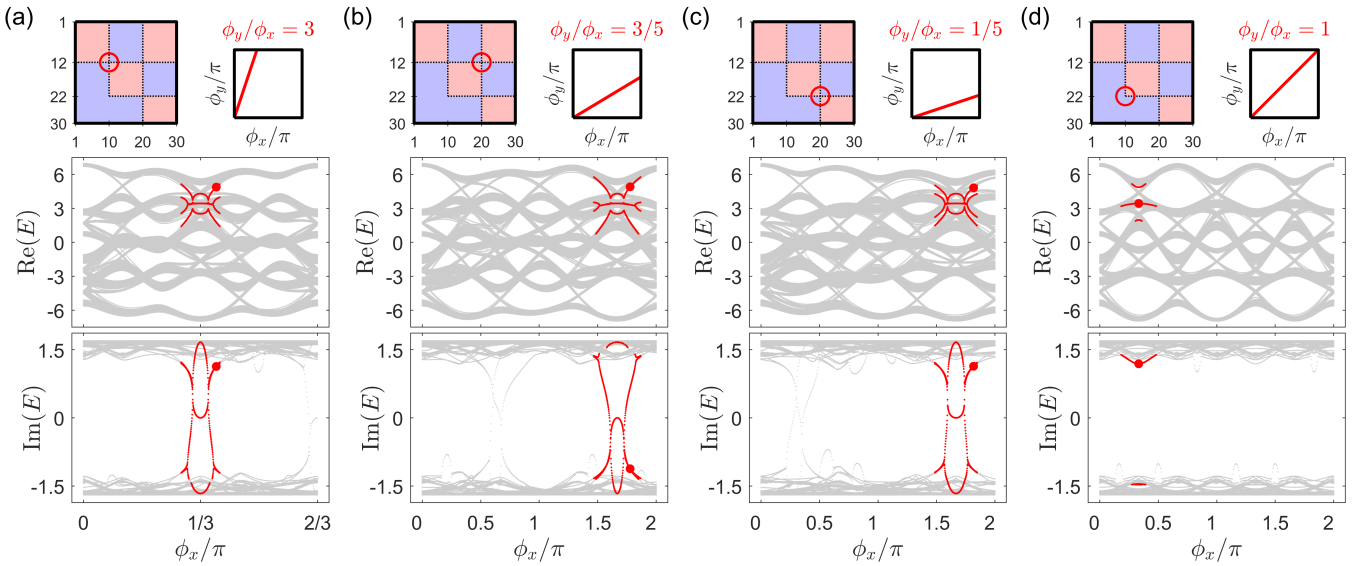

FIG. S11. Spectrums on different planes in the ϕ-space. The configuration is given in Fig. 5 in the main text. Such configuration forms three cross-shaped domain walls and a domain corner. Each of them supports localized corner modes, though in different subspaces of the whole phasespace.

Let's focus on corner states with positive real parts of eigenenergies. This requires two 1D domain-induced edge states $|\chi_{x,y}^{\mathrm{NH}}\rangle$ both have positive real eigenenergies. In the case $\beta = 1/3$, a 1D non-Hermitian AAH chain with a domain wall between site N_1 and N_1+1 (see Fig. 1(a) in the main text) supports domain-induced edge states at the neighborhood of $\phi = \pi, \pi/3, 5\pi/3$ when $N_1 + N = 0, 1, 2 \pmod 3$, respectively.

Fig. S11 shows spectrums confined on four different planes in the phasespace. Sine each subsystem supports sufficiently localized corner states, which is nearly decoupled with the edge and bulk states in the same subsystem, the behaviors at each cross-shaped domain wall is independent of domains away from it. Take case (a) as an example. The behavior in the red circle is nearly the same as the system we studied in the main text, but with $N_1 = 12, N_2 = 10$. Notice that $N_1 + N_y = 0 \pmod 3$ and $N_2 + N_x = 1 \pmod 3$, $|\chi_y^{\mathrm{NH,edge}}\rangle$ will appear at the neighborhood of $\phi_y = \pi$, while $|\chi_x^{\mathrm{NH,edge}}\rangle$ at the neighborhood of $\phi_x = \pi/3$. And we do have found domain-induced corner states on the plane $\phi_y = 3\phi_x$.

Based on these considerations, effective Hamiltonians which describe case (a)-(c) have the same form as Eq. (S7) (for case (b), one should change γ to $-\gamma$). So, in each case we can find a similar structure as we studied in Fig. 3 in the main text, which represents domain-induced corner states localized at the real space (in the red circle). Besides, The red dots in spectrums mark the chosen states whose corresponding field distributions are exhibited in Fig. 5 in the main text.

L-shaped domain walls

The situation in Fig. S11(d) is totally different from the cross-shaped case and need to be analyzed separately. Based on our method, states localized around $(m = 22, n = 12)$ are originate from the coupling of localized states belonging to two subsystems that make up this domain corner. Fig. S12(a) shows an equivalent configuration for more convenient studies (this configuration support localized corner states in the same subspace as Fig. S11(d)). Fig. S12(b) shows ϕ-spectrums of subsystems H_1 and H_2 around $\phi_x = \phi_y = \pi/3$. States localized at the target corner are colored in red. It should be noticed that, H_1 actually does not support topological protected corner modes. The corner modes (P_{1b} and another colored state at $\phi_x = \pi/3$) is actually limiting cases of the topological protected edge modes, which can be easily seen from the three exhibited density plots in Fig. S12(b). However, we'll see later that our method to construct effective Hamiltonians doesn't just apply to the topological case.

Fig. S12(c) shows the ϕ-spectrum of the whole system. One can see there are three domain-induced localized corner modes in total for each proper ϕ_x. In a rough approximation, the effective Hamiltonian that describe these three states should have the form of

$$H = \begin{pmatrix} \omega_{H_1}^1 - i\gamma & 0 & \kappa_1 \\ 0 & \omega_{H_1}^2 - i\gamma & \kappa_2 \\ \kappa_1 & \kappa_2 & \omega_{H_2} + i\gamma \end{pmatrix} \tag{S11}$$

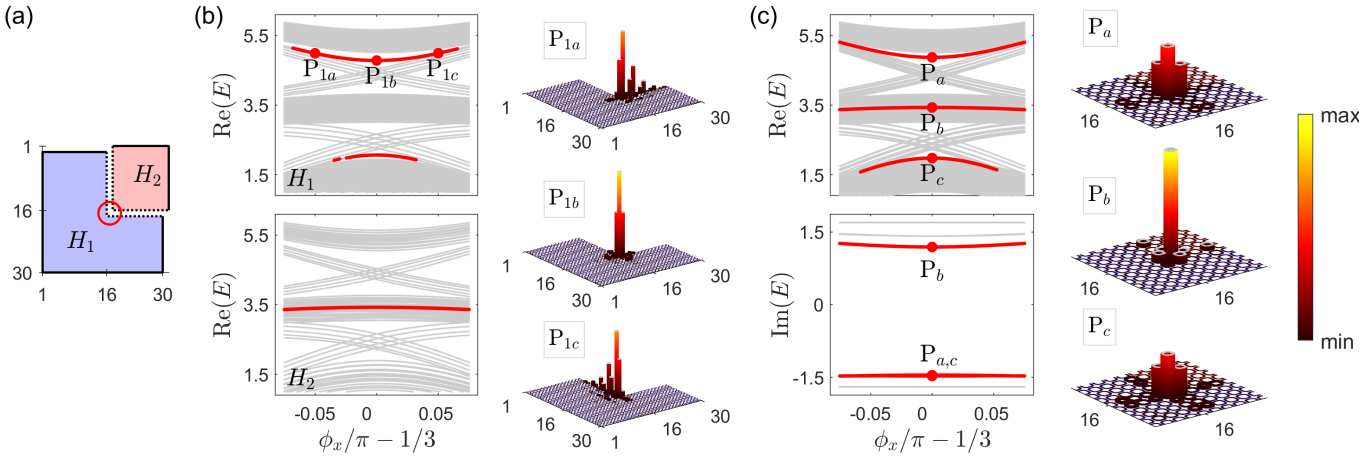

FIG. S12. (a) An equivalent configuration of Fig. S11(d). We also have $N_1 + N_y = 1$ (mod 3) and $N_2 + N_x = 1$ (mod 3) here. (b) Spectrums of two subsystems, the bands colored in red are actually edge bands but not corner bands (as in Fig. S6(c)). (c) Spectrum of the whole non-Hermitian AAH model and density plots of three localized staets at $\phi_x = \pi/3$.

Further more, we should have $\kappa_{1,2} \approx 0$ here, since they are in the similar case as κ_{13} in Eq. (S7). So, as we have seen, three domain-induced localized modes almost behave the same as when two subsystems are separated.

Smaller gain-loss domains

One may ask whether the physical picture will change if the gain or loss is added only close to the center of the cross. Or in the limiting case, what if the gain or loss is only added to the 4 sites at the 4 corners? When gradually reducing the regions with gain or loss (just as we show in Fig. S13), domain-induced corner states (or we should call them gain-loss induced corner states, more generally) still exist. These states do originate from the coupling of edge or corner modes belonging to different subsystems. However, the corresponding effective Hamiltonian may not have the same form as 2D case in Eq. (S7), but with higher dimensions.

To understand this, notice that we can write $H_{\text{eff}}^{\text{2D}}$ in a 4×4 form, because the four basis ψ_i are nearly decoupled with other bulk or edge states in the corresponding subsystem. This fact may not be true when the size of these subsystem are reduced. In

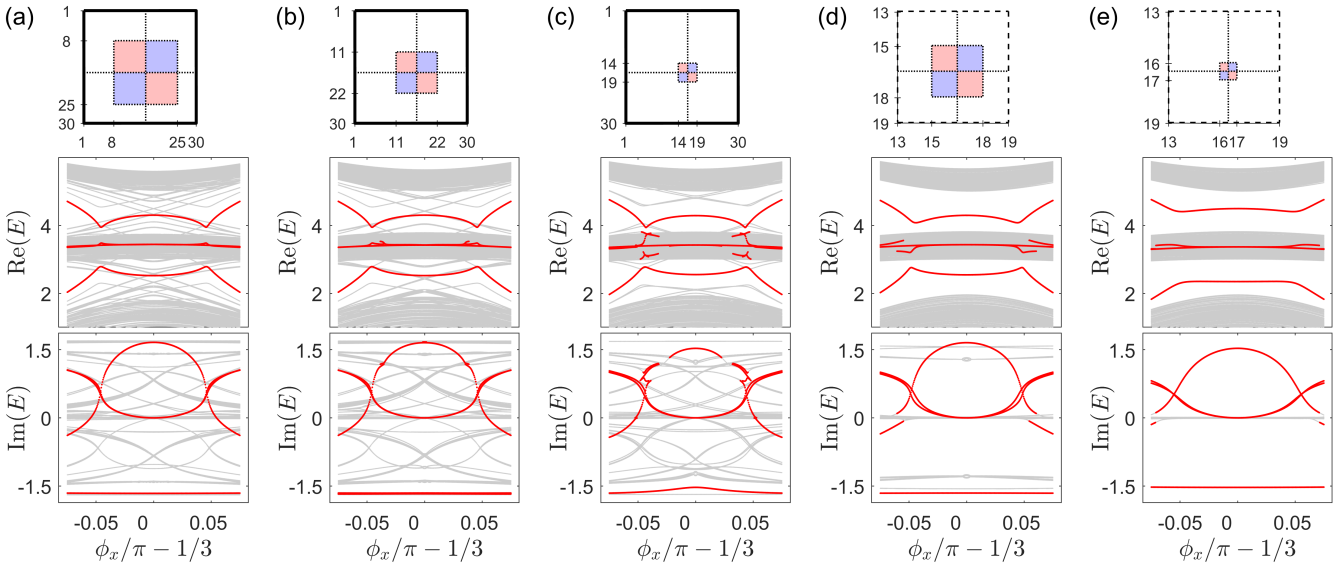

FIG. S13. Spectrums of systems with cross-shaped gain-loss domain walls of different sizes. In each case, the cross-shaped domain wall is centered at $N_1 = N_2 = 16$ and the total non-Hermitian region has a square shape with the length of side $L = 18, 12, 6, 4, 2$ for (a)-(e), respectively. The red bands represent states whose energies distribute most on the four middle sites (N_1, N_2), $(N_1, N_2 + 1)$, $(N_1 + 1, N_2)$ and $(N_1 + 1, N_2 + 1)$.

this case, the dimension of the Hilbert space needs to be increased to get a more proper description for the behaviors at the center. In addition to this, if the non-Hermitian region is getting smaller, two 'domain walls' may be very close to each other. This may result in misjudgements of our target states. For example, the bands colored in red in Fig. S13 represent states $\psi(m,n)$s that satisfy $|\psi(N_1,N_2)|^2+|\psi(N_1,N_2+1)|^2+|\psi(N_1+1,N_2)|^2+|\psi(N_1+1,N_2+1)|^2>\alpha_{th}$, where α_{th} is a preset threshold. Those messy dots in Fig. S13(c) and (d) come from this effect, since two close 'domain walls' interfere with the program's judgment.

The case in Fig. S13(e), that is, the limiting case, seems simple. After all, it has only four colored bands. However, such simple band structure is just a facade. According to the logic we've always worked on, when the non-Hermitian region only contains the middle four sites, the 'domain wall' should be made up of the middle 4 sites with gain or loss and the around 12 Hermitian sites. The colored bands only represent states whose energies tend to describe in the non-Hermitian region, while those states whose energies tend to distribute in the Hermitian region are not highlighted. A (at least) 16-dimensiona1 effective Hamiltonian is necessary for more accurate descriptions of such limiting case.

EP3 composed of domain-induced corner states

A simple EP3 can be described by the following Hamiltonian

$$H_{\mathrm{EP3}}^{\mathrm{eff}}=\begin{pmatrix}\omega+i\gamma & \kappa_1 & \eta\\ \kappa_1 & \omega & \kappa_2\\ \eta & \kappa_2 & \omega-i\gamma\end{pmatrix} \tag{S12}$$

The EP3 appears when $\kappa_1=\kappa_2=\kappa,\eta=0$ and $\gamma=\sqrt{2}\kappa$, in which case all eigenstates coalesce at $(-1,i\sqrt{2},1)^{\mathrm{T}}$ and with the same eigenenergy ω. Start from Eq. (S12), we can design a system, in which the domain-induced corner modes form an EP3. Fig. S14(a) shows such a design. Three domains I-III are experiencing gain$(+i\gamma)$, no gain or loss, and loss$(-i\gamma)$, respectively. The couplings between adjacent domains are denoted by t_1, which is a tunable parameter (and the couplings inside each domain are still $t=1$). On site terms are specially designed to make sure that three basis have the same eigenenergy. Define

$$\Omega^{\pm}(x,q)=V\cos[\pm 2\pi\beta(x-q)+\phi] \tag{S13}$$

On-site potentials of each subsystem are chosen as

$$\Omega^{\mathrm{I}}_{n,m}=\Omega^{-}(n-N_2,0)+\Omega^{+}(m,2),\quad \Omega^{\mathrm{II}}_{n,m}=\Omega^{+}(n,2)+\Omega^{+}(m,2),\quad \Omega^{\mathrm{III}}_{n,m}=\Omega^{+}(n,2)+\Omega^{-}(m-N_1,0) \tag{S14}$$

Such symmetrical design also ensures $\kappa_1=\kappa_2$ in Eq. (S12).

Fig. S14(b) shows the $E-\gamma$ relations of different t_1. When $t_1=1.5$, the $E-\gamma$ relation given by the tight-binding calculation behaves as $\eta>0$ in Eq. (S12), while for $t_1=1.9$ it is just in the opposite case. Since the parameters should change continuously, there must be a critical t_1, which results in $\eta=0$. We find the critical values are $t_1\approx 1.72$ and $\gamma_c\approx 2.317$. We also calculate the related κ through our fitting method, that is, $\kappa_{\mathrm{fit}}=\kappa_{21}=\kappa_{23}=\langle\psi_1|H_{\mathrm{EP3}}|_{\gamma=0}|\psi_2\rangle$, and it gives $\kappa_{\mathrm{fit}}\approx 1.635$. $\gamma_c/\kappa_{\mathrm{fit}}=1.417\approx\sqrt{2}$, which proves that our fitting method is also valid when couplings between two domains are changed. Fig. S14(c) shows the density plot of one of the three domain-induced corner states (the upper plot) and the density plot of state $-\psi_1+i\sqrt{2}\psi_2+\psi_3$. Above calculations show that three domain-induced corner states can be correctly described by Eq. (S12), which has an EP3 form under suitable parameters.

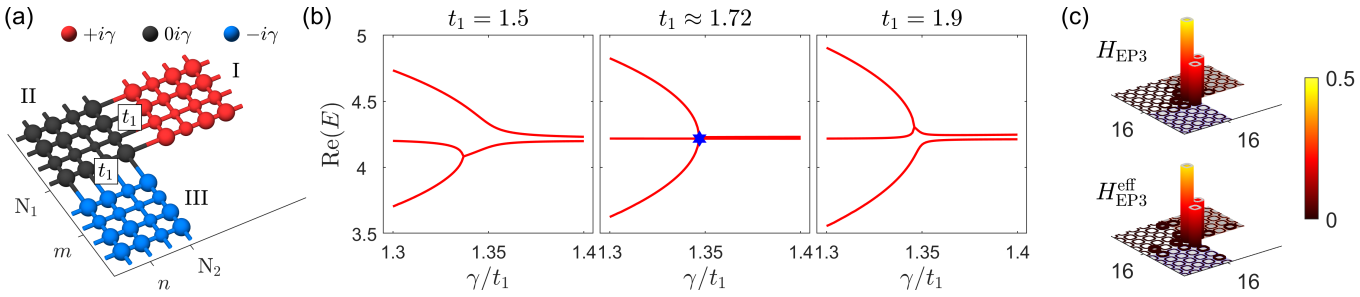

FIG. S14. (a) Schematic plot of our system to realize an EP3. The whole system are symmetric about line $n=m$. (b) $E-\gamma$ relations of three domain-induced corner states with different t_1. The bule star marks an approximate EP3 (since an EP3 is very sensitive to parameters, it is hard to get the true critical t_1 numerically). (c) Field distributions of states given by the tight-binding calculation and the theoretical EP3 eigenstate $(-1,i\sqrt{2},1)^{\mathrm{T}}$.

VI. MODELING AND NUMERICAL SIMULATION

The numerical simulation of our systems is performed using the finite element method (COMSOL Multiphysics®) to demonstrate the validity of our theoretical calculations. All the simulations were done in the 2D case to save computational resources. Out of the consideration of our system, we need to fix the coupling between two adjacent sites, and quantitatively control the eigenfrequency of each site at the same time. We choose the rounded square ring with an adjustable refractive index at its corners as our basic site (see Fig. S15(a)). The refractive index of the four corners is set to $n+i\gamma$ (colored blue) while for four edges (colored gray), it is set to a constant 2.8 (notice that in the software, $\gamma>0$ implies loss, which is different from the convention in the main text). We focus on the eigenfrequency ω of the single ring with a particular WGM order. Fig. S15(b) and (c) show the $n-\mathrm{Re}(\omega)$ relation and the $\mathrm{Im}(\omega)-\gamma$ relation, respectively. The results demonstrate that the above two groups of variables are linear. We also find that the effects of n and γ on ω are decoupled, that is, we can control $\mathrm{Re}(\omega)$ (or $\mathrm{Im}(\omega)$) by changing only n (or γ). Double-rings simulation is also done. We find that the variation of coupling between two neighbor rings is at least two orders less than the variation of ω when we change n and γ. So, it's reasonable to treat the coupling as a constant when adjusting the refractive index.

Simulation for the 1D case

We construct a chain with 24 basic rings, and the gaps between adjacent rings are the same. We choose a certain sequence of refractive index $\{n\}$ such that the frequency of the ring has the following form

$$\mathrm{Re}(\omega_p)=\omega_0+\omega_x\cos(4\pi p/3+\phi),\quad p=1,2,\cdots,24 \tag{S15}$$

Where $\omega_0=1.9379\times10^{14}$ Hz, $\omega_x=2\times10^{11}$ Hz (see Fig. S15(b)) and ϕ is chosen as $(5/3+0.005)\pi$. Besides, we set the imaginary part of the complex refractive index $\gamma=-0.002$ for the first 11 rings, and for the remaining rings we set $\gamma=0.002$ ($N_1=11$, see Fig. 1(b) in the main text). We find two domain-induced states by using the eigenfrequency module of COMSOL Multiphysics®, which are exhibited in Fig. S16. The results of the simulation match the theoretical one shown in Fig. 2 in the main text.

Simulation for the 2D case

For the 2D case, we construct a lattice with 12×12 basic rings and we choose their refractive index n to make their eigenfrequencies satisfy

$$\omega_{p,q}=\omega_0+\omega_x\cos(4\pi p/3+\phi)+\omega_y\cos(4\pi q/3+\phi),\quad p,q=1,2,\cdots,12 \tag{S16}$$

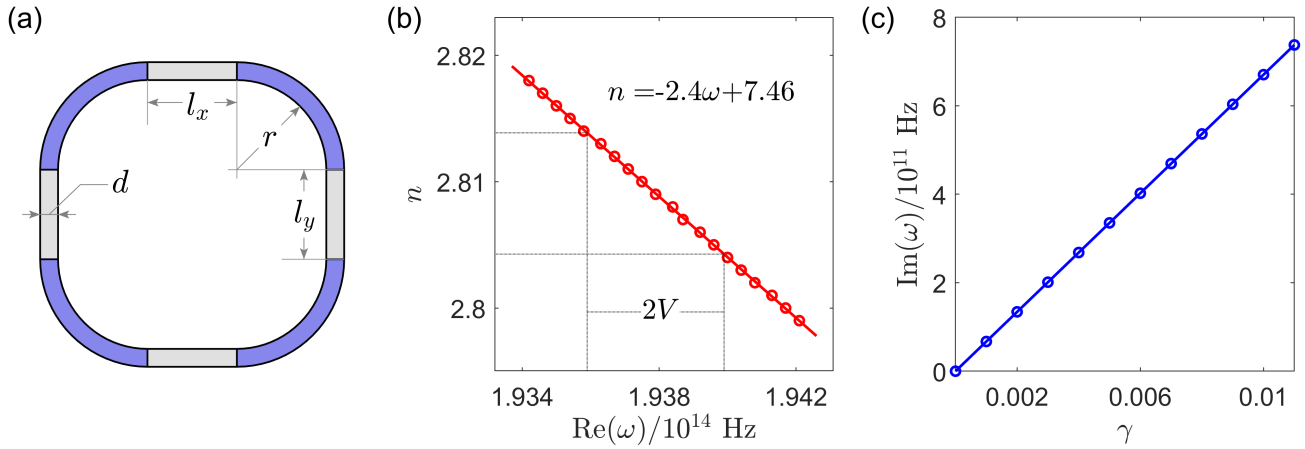

FIG. S15. (a) Schematic plot of our unit ring. We employ $d=500$ nm, $l_x=l_y=r=5000$ nm. The refraction index at four corners (printed blue) is adjustable, while for four edges (printed gray), the refractive index is fixed to 2.8. (b) The fitting curve of the real part of the refractive index n and the single-ring eigenfrequency $\mathrm{Re}(\omega)$, which shows a good linear relationship between them. Only frequencies in a certain range are considered in the following step, which is centered at 1.9379×10^{14} Hz and has a widening of 4×10^{11} Hz ($2V$ in the plot). (c) The fitting curve of the single ring loss $\mathrm{Im}(\omega)$ and the imaginary part of the complex refractive index γ.

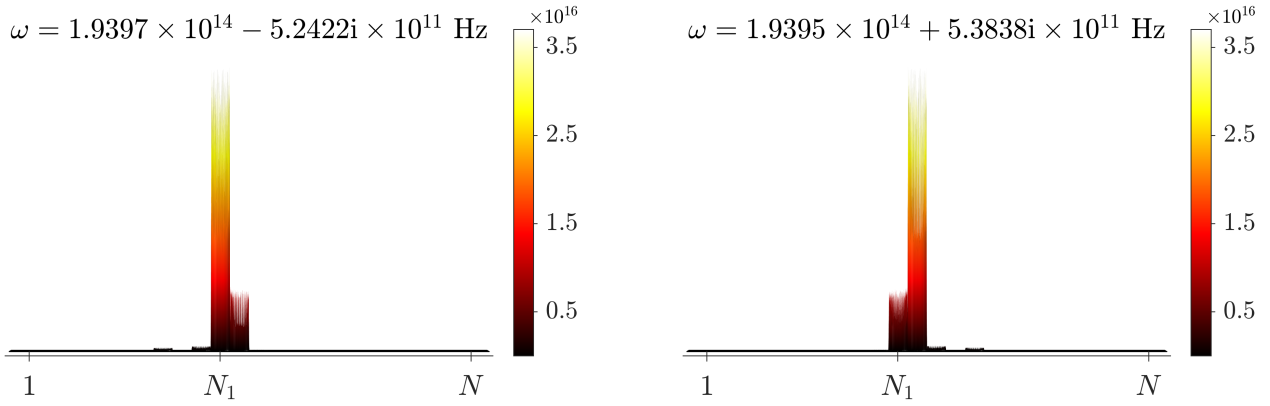

FIG. S16. The square of the modulus of the electric field $|E|^2$, which is corresponding to the normalized field distribution in the main text, is shown in the form of the height diagram. The title of each plot gives the corresponding eigenfrequency. (a) The state with a negative imaginary eigenfrequency, which tends to distribute in the gain region. (b) The state with a positive imaginary eigenfrequency, which tends to distribute in the loss region.

Which is consistent with Eq. (3) in the main text with $N_x + N_y = 12$, $\beta_x = \beta_y = 1/3$, $\phi_x = \phi_y = \phi$. We set $\omega_0 = 1.9379 \times 10^{14}$ Hz, $\omega_x = \omega_y = 1 \times 10^{11}$ Hz ($V/2$ in Fig. S15(b)) and $N_1 = N_2 = 6$ (see Fig. 3(a) in the main text). The imaginary part of the refractive index is set to $-\gamma$ for domain II and IV, while for the remaining part, it is set to $+\gamma$. As we have shown in the last subsection of Sec. IV, such a configuration supports domain-induced corner states in the neighborhood of $\phi_x = \phi_y = \pi$. Three groups of parameters are chosen in the simulation, which are

a. $\phi = 1.005\pi$, $\gamma = 0.002$.
b. $\phi = 1.005\pi$, $\gamma = 0.004$.
c. $\phi = 1.05\pi$, $\gamma = 0.004$.

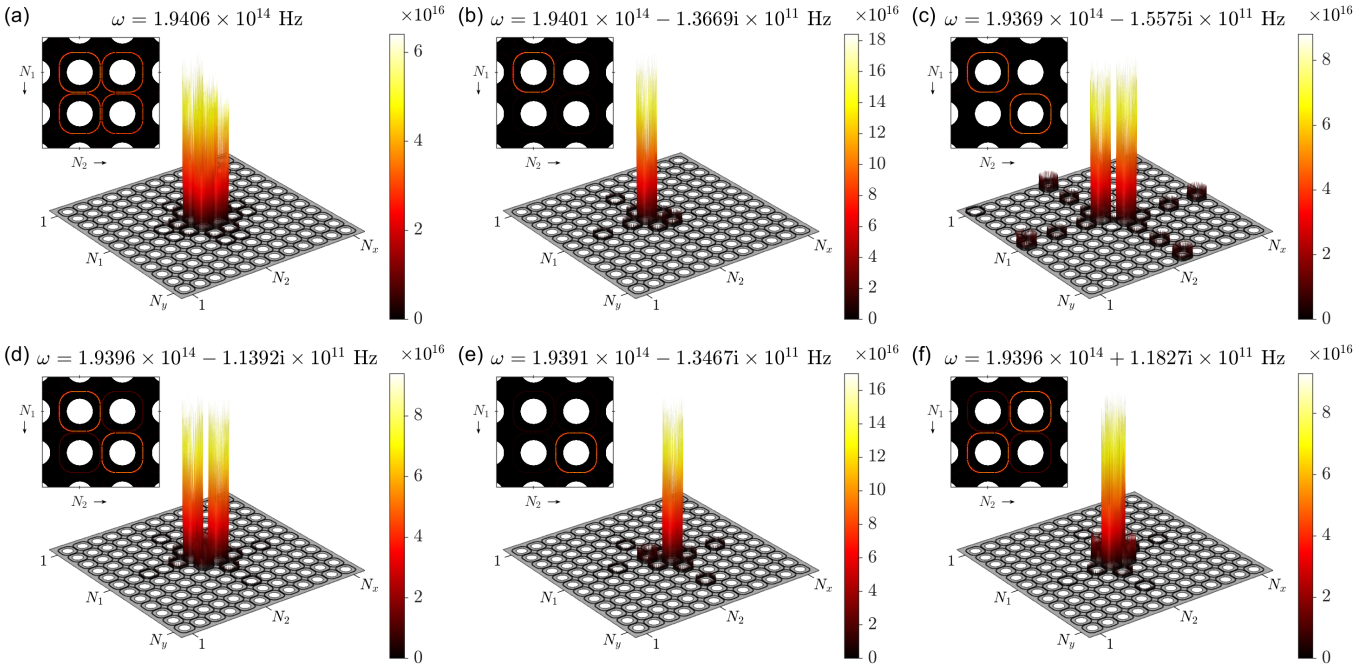

FIG. S17. Height diagrams of $|E|^2$ of six domain-induced corner states with type P_{1-6}. The inner plot zooms in on four rings (N_1, N_2+1), (N_1, N_2), (N_1+1, N_2) and (N_1+1, N_2+1), which are rings near the intersection of the domain wall. (a) Q_{a1}-typed state shown in Fig. S8, which represents the PT-unbroken phase near $\phi = \pi$. (d) Q_{b1}-typed state, which represents the PT-broken phase near $\phi = \pi$. (b)(e) P_3-typed states shown in Fig. 4(e) in the main text, which are found away from $\phi = \pi$. (c) Q_{a4}-typed state, which has a rather large imaginary part compared to the other five states. (f) P_4-typed state shown in Fig. 4(e) in the main text, which nearly has a probability density $(1/2,0,1/2,0)^{\mathrm{T}}$. All of the field distributions and frequency characteristics are well compounded with theoretical calculations in the main text.

We do find several representative states and some of the simulation results are exhibited in Fig. S17. To be more precise, Fig. S17(a) is found in case a, Fig. S17(c), (d) are found in case b, Fig. S17(b), (e), (f) are found in case c. In general, the simulated field distribution and eigenfrequency properties agree well with the theoretical results in the main text, which proves the validity of our theoretical calculation.

* These authors contribute equally to this work.
† xiaoyonghu@pku.edu.cn
‡ cuicuilu@bit.edu.cn
§ phchan@ust.hk

[1] J.-W. Dong, X.-D. Chen, H. Zhu, Y. Wang, and X. Zhang, Nature Materials **16**, 298 (2017).
[2] L.-H. Wu and X. Hu, Phys. Rev. Lett. **114**, 223901 (2015).
[3] Y. E. Kraus and O. Zilberberg, Phys. Rev. Lett. **109**, 116404 (2012).
[4] Z.-G. Chen, W. Zhu, Y. Tan, L. Wang, and G. Ma, Phys. Rev. X **11**, 011016 (2021).